ACCSCIENCE PUBLISHING

International Journal of Bioprinting

RESEARCH ARTICLE

Data-driven design and mechanical validation of three-dimensional-printed biphasic osteochondral scaffolds with interlocking interface using Ti6Al4V

Yi Tang[1†], Zhenlan Xia[2†], Jing Zeng[3†], Rui Zhu[2], Chengyue Yan[2], Tengfei Fan[2], Yupeng Hu[2], Zhuoxuan He[2], Yuanlong Li[4*], Zhao Wang[2*], and Jun Tang[1*]

[1]Department of Orthopedics, The Second Affiliated Hospital of Wenzhou Medical University, Wenzhou, Zhejiang, China

[2]Department of Orthopaedic Surgery, Guangzhou Key Laboratory of Spine Disease Prevention and Treatment, Guangdong Provincial Key Laboratory of Major Obstetric Diseases, Guangdong Provincial Clinical Research Center for Obstetrics and Gynecology, The Third Affiliated Hospital, Guangzhou Medical University, Guangzhou, Guangdong, China

[3]Department of Orthopedics, Liwan Central Hospital of Guangzhou, Guangzhou, Guangdong, China

[4]Department of Orthopaedics, Sun Yat-Sen Memorial Hospital, Sun Yat-Sen University, Guangzhou, Guangdong, China

[†]*These authors contributed equally to this work.*

***Corresponding authors:**
Yuanlong Li
(liylong53@mail.sysu.edu.cn);
Zhao Wang
(z.wang@gzhmu.edu.cn);
Jun Tang
(195018@wzhealth.com)

Citation: Tang Y, Xia Z, Zeng J, *et al*. Data-driven design and mechanical validation of three-dimensional-printed biphasic osteochondral scaffolds with interlocking interface using Ti6Al4V. *Int J Bioprint*. 2026;12(4):026220222. doi: 10.36922/IJB026220222

Received: May 28, 2026

Revised: June 5, 2026

Accepted: June 22, 2026

Published online: June 25, 2026

Copyright: © 2026 Author(s). This is an Open-Access article distributed under the terms of the Creative Commons Attribution License, permitting distribution, and reproduction in any medium, provided the original work is properly cited.

Publisher's Note: AccScience Publishing remains neutral with regard to jurisdictional claims in published maps and institutional affiliations.

Abstract

Osteochondral defects require biomimetic scaffolds. These scaffolds must simultaneously reproduce the mechanical heterogeneity of subchondral bone and maintain stable integration between bone and cartilage. In this study, we developed a data-driven design and validation framework for patient-specific biphasic Ti6Al4V osteochondral scaffolds using public computed tomography (CT) datasets and finite element optimization. CT images from the Osteoarthritis Initiative database were analyzed to extract Hounsfield unit (HU) distributions and derive anisotropic mechanical parameters through density–elasticity mapping, yielding three representative design targets corresponding to low-, medium-, and high-density cancellous bone. Gradient Gyroid scaffolds with region-specific porosity and strut parameters were subsequently designed to match these physiological targets. To improve osteochondral integration, an interlocking interface architecture incorporating peg-based mechanical anchoring was optimized using parametric finite element response surface modeling and Bayesian optimization. The scaffolds were fabricated via selective laser melting using Ti6Al4V powder and comprehensively characterized through quasi-static compression, hemispherical indentation, and interface shear testing. The fabricated scaffolds exhibited high geometric fidelity, with average dimensional deviations of less than 0.15 mm. The measured macroscopic compressive moduli demonstrated excellent manufacturing fidelity, deviating by less than 10% from the CT-derived design targets across all density groups, thereby offering a viable path to mitigate clinical stress shielding. Furthermore, the optimized interlocking interface significantly increased both indentation stiffness and destructive interface shear strength relative to smooth-interface controls ($p < 0.01$), closely matching finite element predictions of minimized stress concentration at the osteochondral junction. Taken together, these findings demonstrate that CT-informed, topology-optimized Ti6Al4V scaffold architectures

can achieve precisely matched porous mechanics while substantially expanding interface stability, providing a highly reproducible and translatable strategy for personalized load-bearing joint repair applications.

Keywords: Osteochondral scaffold; Ti6Al4V; Gyroid lattice; Interlocking interface

1. Introduction

Osteoarthritis and traumatic osteochondral defects impact millions of individuals globally, with an estimated prevalence surpassing 10% among the adult population.[1] Articular cartilage injuries often penetrate into the subchondral bone, giving rise to intricate defects that necessitate the simultaneous regeneration of two distinct tissues as an integrated functional entity.[2,3] Current clinical therapies include autologous grafting, allografts, and total joint replacement. However, they are constrained by donorsite morbidity, risks of disease transmission, and longterm complications such as aseptic loosening and stress shielding.[4-6]

Tissue engineering offers a promising alternative by providing temporary scaffolds that facilitate endogenous cell infiltration and tissue regeneration.[7] Among the fabrication techniques, three-dimensional (3D) printing enables the production of patient-specific implants with precisely controlled external geometries and internal architectures.[8-10] In osteochondral applications, 3D printing allows for the fabrication of multiphasic scaffolds with region-specific properties: a load-bearing bone phase that mimics cancellous bone and a compliant chondral phase that replicates articular cartilage.[11,12]

Despite these advancements, two fundamental challenges remain unaddressed. First, mechanical matching: scaffolds are required to replicate the anisotropic mechanical behavior of native bone to prevent stress shielding. Natural cancellous bone demonstrates substantial regional variation in elastic modulus (50–1,500 MPa) and a high degree of anisotropy (DA ≈ 0.6–0.7), which reflects its adaptation to physiological loading.[13,14] Conventional uniform architectures fail to capture this heterogeneity. Although functionally graded structures have been introduced,[15,16] most of them rely on empirical parameter selection rather than patient-specific mechanical data obtained from clinical imaging. Second, interface integration: the junction between the osteal and chondral phases represents a critical weak point that is prone to delamination under shear and tensile stresses encountered during joint loading.[17,18] Despite the mechanical demands of articulation, quantitative interface strength testing is conspicuously absent in most 3D-printed osteochondral scaffold studies.[19] Recent reviews emphasize that although reinforcement strategies exist (e.g., chemical bonding, solvent casting, mechanical interlocking), systematic evaluation using standardized shear tests is lacking.[20,21]

An additional opportunity lies in public repositories of clinical computed tomography (CT) data, such as the Osteoarthritis Initiative (OAI), which contain thousands of high-resolution scans along with corresponding demographic information. These databases offer an untapped resource for extracting population-level bone mechanical properties, establishing relationships between Hounsfield units (HU) and strength, and generating design targets for patient-specific scaffolds.[22-24] Recent work by Schreiber *et al.*[23] demonstrated the feasibility of mapping HU to strength via rational Bézier curves and translating the resulting curves into lattice parameters using octree-based adaptive subdivision. However, such approaches have not been systematically integrated with experimental validation of mechanical equivalence using cost-effective materials such as Ti6Al4V.

Ti6Al4V alloys have become one of the most widely utilized metallic biomaterials for load-bearing orthopedic implants due to their excellent biocompatibility, corrosion resistance, and high mechanical strength.[25,26] With the development of additive manufacturing technologies such as selective laser melting (SLM), porous Ti6Al4V scaffolds with controlled lattice architectures can now be fabricated with high geometric accuracy and tunable mechanical properties.[27] Significantly, the introduction of controlled porosity and biomimetic lattice structures substantially reduces the effective elastic modulus of Ti6Al4V, alleviating stress shielding while maintaining sufficient structural integrity for load-bearing applications.[28,29] Recent studies have shown that Gyroid and triply periodic minimal surface (TPMS)-based Ti6Al4V scaffolds exhibit favorable permeability, mechanical isotropy, and osseointegration potential.[30] However, most current studies rely on empirically selected architectures rather than patient-specific mechanical targets derived from clinical imaging.

To address these critical limitations, we developed a clinically informed, data-driven framework to guide the topological design and mechanical validation of biphasic

Ti6Al4V osteochondral scaffolds. This framework seamlessly bridges clinical radiographic data and additive manufacturing by leveraging publicly available OAI datasets to map patient-specific cancellous bone targets, which are then translated into functionally graded Gyroid lattices with region-specific porosity and structural anisotropy. To ensure structural integrity at the osteochondral junction, a biomimetic interlocking interface was parametrically optimized and subsequently validated using a closed-loop platform that combined computational finite element simulations with destructive experimental testing, including compression, indentation, and interface shear characterization. We hypothesized that these topology-optimized titanium scaffolds could successfully downscale intrinsic metallic rigidity to physiological targets while simultaneously elevating interfacial shear resistance far beyond that of conventional smooth-interface controls (Figure 1).

2. Materials and methods

2.1. Computed tomography image analysis and mechanical mapping

A cohort of 30 subjects from the OAI database (proximal femur CT scans, slice thickness ≤1 mm, no metal artifacts) was used for HU analysis and mechanical property mapping. The HU threshold (150–700 HU) was based on published ranges for trabecular bone in the proximal femur.[23] Segmentation of cancellous bone regions (femoral head and neck) was performed in 3D Slicer (version 5.6) using thresholding (150–700 HU). Mean HU values were extracted for each region of interest (ROI). Anisotropic mechanical parameters were calculated using the powerlaw equations established by Naghavi *et al.*[28] for principal elastic moduli (E_1, E_2, E_3), shear moduli, and yield strengths. The control points of the rational Bézier curve P_0 (60,0.1), P_1 (675,16), P_2 (928,130), P_3 (1760,200), and weights [1,50,50,1] were selected to best fit the pooled HUstrength data from our OAI subset, achieving an R^2 of 0.94.[28] A rational Bézier curve with control points P_0 (60, 0.1), P_1 (675, 16), P_2 (928, 130), P_3 (1760, 200), and weights [1, 50, 50, 1] was constructed to model the HU–strength relationship. Kmeans clustering was applied to classify ROIs into low, medium, and highdensity groups based on HU values.

All CT scans followed the OAI acquisition protocol (Siemens SOMATOM Definition, Siemens, Germany; 120 kVp, 200 mAs, slice thickness 0.625 mm reconstructed to 1 mm). ROIs were manually contoured on every fifth slice within the femoral head and neck, excluding trabecular bone within 1 mm of the cortical shell to avoid partial volume effects.

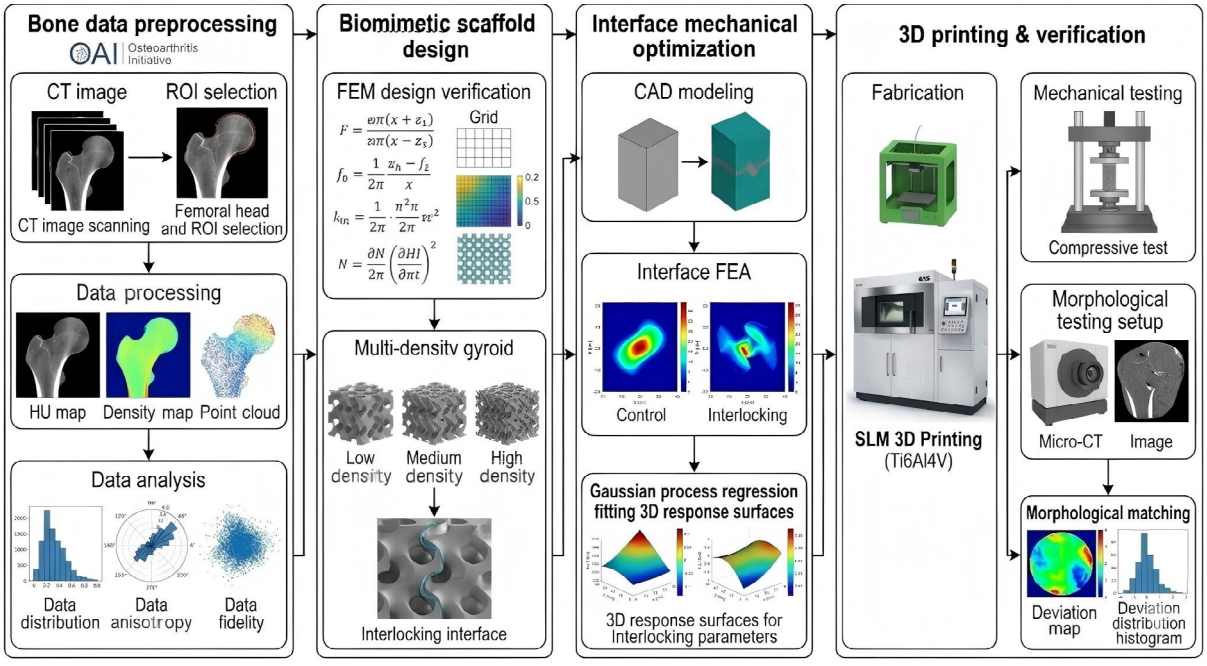


Figure 1. Schematic overview of the data-driven pipeline. The workflow includes computed tomography (CT) database analysis for bone data preprocessing and mechanical mapping; biomimetic multi-density Gyroid scaffold design with an optimized interlocking interface; selective laser melting (SLM) three-dimensional (3D) printing using Ti6Al4V; and comprehensive morphological and mechanical verification (including micro-CT imaging and compressive testing).

2.2. Osteoarthritis Initiative data screening and morphological analysis

The OAI database was queried for subjects with complete 3D dual-echo steady-state magnetic resonance imaging acquired using a 3.0-T Siemens Magnetom Trio scanner (Siemens Healthcare, Germany; slice thickness ≤1 mm) and available Kellgren–Lawrence (KL) grading. Subjects with metal artifacts or incomplete proximal femur coverage were excluded. From the remaining 2,134 subjects, we performed stratified random sampling according to KL grade (0–4) to obtain 100 subjects per grade ($n = 500$). For each subject, the femoral condyle, tibial plateau, and meniscus were semiautomatically segmented using a U-Net-based algorithm (Dice coefficient >0.85) and reconstructed into 3D surface models (STL format). All models were rigidly aligned to a common reference via Procrustes superimposition.

2.3. Statistical shape model and principal component analysis

A statistical shape model was built from the 500 aligned femoral and tibial surfaces using point distribution models. Principal component analysis was performed to reduce dimensionality, retaining the first 10 principal components, which explained >80% of the total shape variance. For each principal component, shape variations at ±3 standard deviations from the mean were visualized as colorcoded displacement maps (red: outward, blue: inward). The resulting principal component scores were used for subsequent clustering and template generation.

2.4. Morphological clustering and interface template extraction

Kmeans clustering was applied to the first 10 principal component scores to identify distinct morphological phenotypes of the subchondral bone interface. The optimal number of clusters ($k = 3$) was determined by the elbow method and silhouette coefficient (mean silhouette = 0.62). For each cluster, the mean shape was calculated and used as a representative "interface design template." Three geometric parameters were extracted from each template: interface curvature radius (mm), cartilage thickness (mm), and bone depression depth (mm). Differences among clusters were assessed using oneway analysis of variance (ANOVA) with Tukey HSD posthoc test ($\alpha = 0.05$).

2.5. Scaffold design

The Gyroid surface was described by the implicit function $f(x,y,z) = \sin(2\pi x/a)\cos(2\pi y/b) + \sin(2\pi y/b)\cos(2\pi z/c) + \sin(2\pi z/c)\cos(2\pi x/a) = t$, where a, b, c are unit cell dimensions and t controls volume fraction. To map lattice geometry to mechanical properties, finite element analysis (FEA; Abaqus, version 2022) of 60 parameter combinations (unit cell size 3–5 mm, strut diameter 0.2–0.6 mm, anisotropy 0–0.7) was performed. Crucially, standard Ti6Al4V material properties (E = 110 GPa, ν = 0.33, yield strength = 950 MPa) were utilized to establish a structure–property scaling law. The fitted scaling law from the 60 FEA simulations was $E_{eq}/E_s = 0.88 \cdot (VF)^{1.35} \cdot (DA)^{-0.42}$, yielding a coefficient of determination $R^2 = 0.98$. This scaling law was derived from our FEA simulations and is consistent with previously reported relationships for TPMS lattices. [27,31]

For each density group, the strut diameter and degree of anisotropy were back-calculated to precisely downregulate the bulk stiffness of Ti6Al4V to match the physiological target moduli of cancellous bone.

Recently, datadriven inverse design frameworks have emerged as powerful tools for optimizing complex engineering systems, including tissue engineering scaffolds. For instance, Yu *et al.*[32] employed a multimodal-guided latent diffusion model for the inverse topological design of tissue engineering constructs. Inspired by such approaches, we adopted a Bayesian optimization framework to identify optimal interlocking geometries for our osteochondral scaffold.

2.6. Finite element analysis and design optimization

Finite element analysis was performed in Abaqus (version 2022) using 10node quadratic tetrahedral elements (C3D10). A mesh convergence study was conducted: a global seed size of 0.5 mm was selected, as further refinement changed the predicted stiffness by <2%. The bone phase (Ti6Al4V) was assigned a linear elastic material model with E = 110 GPa, $\nu = 0.33$; the cartilage phase (polycaprolactone [PCL]) with E = 350 MPa, $\nu = 0.30$. The interface between the two phases was modeled as a perfectly bonded tie constraint. A displacementcontrolled compressive load (0.5 mm/min) was applied to the top surface, while the bottom surface was fully constrained (Ux = Uy = Uz = 0). Contact between the indenter and scaffold was frictionless.

2.7. Cartilage phase fabrication

The cartilage phase was fabricated using medicalgrade PCL (Mn = 80 kDa; Polysciences, United States). PCL pellets were melted at 80 °C and injected into a custom silicone mold containing the prepositioned Ti6Al4V bone phase scaffold. The assembly was cooled at room temperature for 24 hours, allowing the PCL to solidify and mechanically interlock with the pegs of the bone phase. No adhesive or chemical bonding agent was used.

2.8. Morphological observation of the fabricated scaffolds

The morphology of the SLM-fabricated Ti6Al4V scaffolds was examined using a stereomicroscope (SZ61, Olympus Corporation, Japan). Representative images were acquired under identical illumination conditions at a magnification of 10×. The dimensional integrity, surface morphology, and interlocking interface geometry of the fabricated scaffolds were qualitatively evaluated by comparing the printed structures with the corresponding computer-aided design models.

2.9. Mechanical testing

All tests were performed on a universal testing machine (Instron 5982, Instron Corp., United States) at 0.5 mm/min. Sample sizes were $n = 5$ per group. For quasistatic compression, bonephase scaffolds (low-, medium-, and high-density) were compressed between flat platens to a 50% strain. Loaddisplacement data were converted to stress–strain curves. Elastic modulus was determined from the linear region (5–20% strain). Yield strength (0.2% offset) and energy absorption (area under the curve) were also recorded. For hemispherical indentation, biphasic scaffolds (mediumdensity bone phase with cartilage phase) were embedded in resin, leaving the cartilage surface exposed. A 5 mm diameter hemispherical indenter was pressed to a depth of 2 mm. Indentation stiffness was calculated from the initial linear portion of the loaddisplacement curve. For the interface shear test, biphasic scaffolds (smooth interface, 30% interlock, 60% interlock) were tested using a custom fixture with a constraining platen.[33] The bone phase was fixed, and a shear load was applied horizontally to the cartilage phase until failure. Interface shear strength was calculated as **Equation 1**:

$$\tau = F_max/A_interface \quad (1)$$

where $A_interface = \pi \cdot (diameter/2)^2$.

2.10. Statistical analysis

Normality of continuous variables was assessed using the Shapiro–Wilk test. Normally distributed data (e.g., elastic modulus, indentation stiffness, interface shear strength) are presented as mean ± standard deviation and were analyzed using ANOVA followed by Tukey's HSD posthoc test for multiple comparisons. Nonnormally distributed data (e.g., osteophyte scores) are presented as median (interquartile range) and were analyzed using the Kruskal–Wallis test with Dunn's posthoc test. Categorical variables (e.g., sex) were compared using Fisher's exact test. Onesample *t*tests were used to compare measured elastic moduli against their paired CTderived target moduli. Pearson correlation coefficients were calculated for the parametric correlation matrix. A significance level of $\alpha = 0.05$ was used for all tests.

3. Results

3.1. Baseline characteristics

Table 1 presents the baseline demographic, radiographic, cartilage morphological, and CT-derived biomechanical characteristics of the 30 subjects selected from the OAI database. Subjects were stratified into three density groups (low, medium, high) based on k-means clustering of HU values extracted from the proximal femur. The groups were balanced with 10 subjects each.

Significant structural and biomechanical differences were observed among the groups, particularly in the HU range and all principal elastic moduli ($p < 0.001$), confirming that the clustering effectively captured distinct bone density profiles. Notably, the target moduli for scaffold design (452, 858, and 1,362 MPa) were derived directly from the mean E_1 of these groups; thus, they serve as downstream design parameters rather than independent baseline characteristics. Finally, no significant differences were found in age, sex, or body mass index, indicating that demographic confounders were well controlled across the three density cohorts.

3.2. Osteoarthritis Initiative data screening and morphological analysis

To obtain populationspecific morphological templates, we screened the OAI database (Figure 2A) and reconstructed 3D joint surfaces (Figure 2B). Principal component analysis of the statistical shape model revealed that the first three principal components explained 72% of the total shape variance (Figure 2C). *t*distributed stochastic neighbor embedding clustering of the shape features showed a clear separation according to KL grade (Figure 2D), confirming that osteoarthritis severity is strongly associated with distinct morphological phenotypes.

From the OAI-derived shape models, we extracted the morphology of the subchondral bone interface. Heat maps (Figure 3A) show a clear gradient of increasing curvature and deepening of the interface as the KL grade advances. K-means clustering identified three distinct interface phenotypes (Figure 3B): flat (Cluster 1; $n = 12$, mean KL: 1.2), mildly depressed (Cluster 2; $n = 18$, mean KL: 2.5), and deeply depressed (Cluster 3; $n = 15$, mean KL: 3.8). Boxplot analysis (Figure 3C) confirmed significant differences in curvature radius, cartilage thickness, and bone depression depth among the three clusters.

Table 1. Baseline characteristics of the study population stratified by bone density group

Characteristics	Overall (N = 30)	Low density (n = 10)	Medium density (n = 10)	High density (n = 10)	p-value
Demographics					
Age (years)	62.4 ± 8.7	60.2 ± 9.1	62.8 ± 8.5	64.1 ± 8.3	0.582
Female, n (%)	16 (53.3)	5 (50.0)	6 (60.0)	5 (50.0)	>0.999
BMI (kg/m²)	28.1 ± 3.9	26.5 ± 3.2	28.3 ± 4.0	29.5 ± 4.1	0.215
Radiographic characteristics					
HU range	98–532	98–215	216–358	359–532	<0.001
JSW (mm)	3.72 ± 1.38	4.15 ± 1.20	3.68 ± 1.35	3.34 ± 1.42	0.402
Osteophyte score (0–12)	3.1 ± 2.5	1.8 ± 1.6	3.2 ± 2.4	4.3 ± 2.8	0.081
Cartilage morphology (MRI)					
Medial femoral thickness (mm)	1.98 ± 0.48	2.21 ± 0.42	1.95 ± 0.45	1.78 ± 0.52	0.134
Lateral femoral thickness (mm)	2.12 ± 0.52	2.35 ± 0.48	2.08 ± 0.50	1.92 ± 0.55	0.165
Subchondral bone curvature (mm^{-1})	0.082 ± 0.034	0.068 ± 0.022	0.085 ± 0.031	0.094 ± 0.038	0.158
Biomechanical parameters (CT-derived)					
E_1 (MPa)†	904 ± 382	452 ± 83	858 ± 117	1,362 ± 175	<0.001
E_2 (MPa)	499 ± 214	283 ± 52	491 ± 68	724 ± 85	<0.001
E_3 (MPa)	270 ± 124	148 ± 31	263 ± 38	398 ± 47	<0.001
Degree of anisotropy	0.69 ± 0.05	0.67 ± 0.04	0.69 ± 0.03	0.71 ± 0.02	0.028

Notes: Data are expressed as mean ± SD, median (IQR), or n (%). E_1, E_2, and E_3 represent CT-derived principal orthotropic moduli; degree of anisotropy = $1-(E_3 / E_1)$.

† The mean E1 values (452, 858, and 1,362 MPa) serve as the bioinspired targets to parameterize the gradient Gyroid architectures for the SLM-fabricated Ti6Al4V scaffolds.

Abbreviations: BMI: Body mass index; CT: Computed tomography; HU: Hounsfield unit; IQR: Interquartile range; JSW: Joint space width; MRI: Magnetic resonance imaging; SD: Standard deviation; SLM: Selective laser melting.

3.3. Computed tomographybased mechanical characterization

Analysis of 30 OAI datasets yielded HU distributions ranging from 98 to 532 HU. K-means clustering based on HU values classified the ROIs into three distinct density groups: low (98–215 HU), medium (216–358 HU), and high (359–532 HU) (Figure 4A, 4B, and 4D).

The representative anisotropic mechanical parameters for each group are summarized in Table 2. Crucially, these parameters were not measured directly but derived from established density-elasticity empirical power-law equations, thereby converting localized HU values into apparent mechanical properties. The rational Bézier curve provided an excellent fit to the HU–strength relationship (R^2 = 0.94 for E_1 prediction), as shown in Figure 4C, with less than 10% deviation at the control points.

Furthermore, the degree of anisotropy was defined mechanically as $1 - (E_3/E_1)$. Although the absolute variation in the degree of anisotropy across the three density groups was relatively small (0.67 to 0.71), these anisotropic targets were explicitly incorporated into the subsequent Gyroid lattice generation to maximize the biomimetic fidelity of the patient-specific scaffolds.

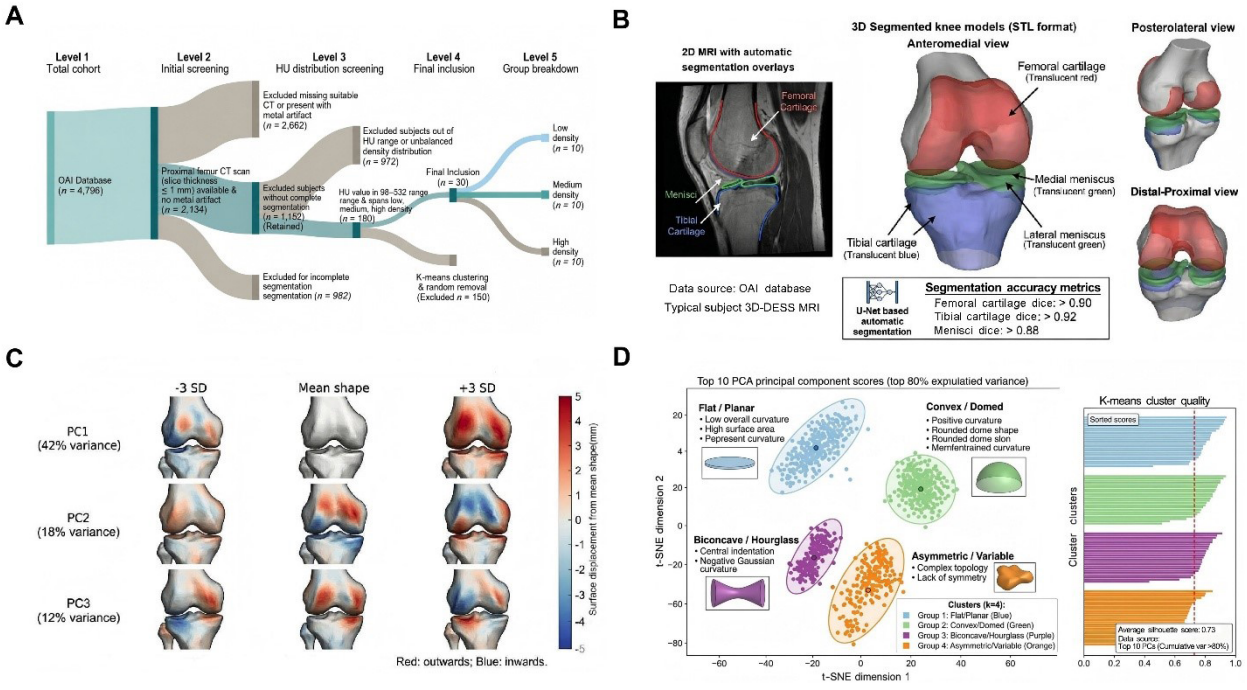


Figure 2. OAI data screening and morphological analysis pipeline. (A) Subject selection flow. (B) Representative 3D surface reconstruction of knee joint tissues. (C) Principal component analysis of the statistical shape model showing the first three shape modes. (D) *t*SNE visualization of morphological clustering by KL grade.

Abbreviations: 3D: Three-dimensional; CT: Computed tomography; KL: Kellgren–Lawrence; MRI: Magnetic resonance imaging; OAI: Osteoarthritis Initiative; PCA: Principal component analysis; SD: Standard deviation; *t*-SNE: *t*-distributed stochastic neighbor embedding.

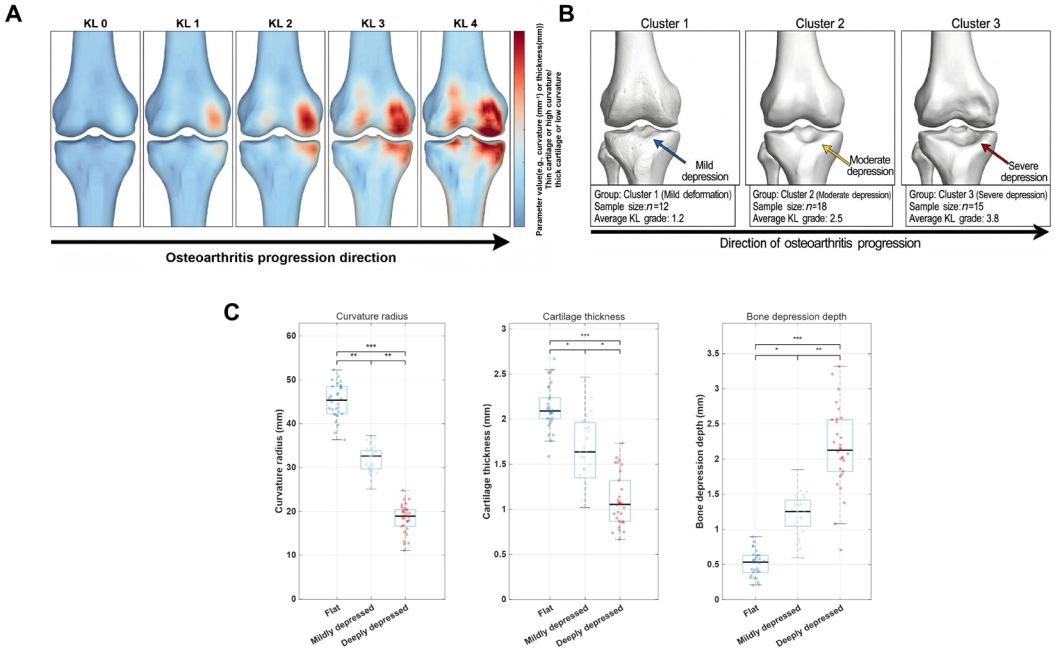


Figure 3. Interface morphology clustering and representative template generation. (A) Heat maps of subchondral bone interface curvature across Kellgren–Lawrence (KL) grades. (B) Three representative interface templates were identified by Kmeans clustering. (C) Boxplots comparing curvature radius, cartilage thickness, and bone depression depth among clusters.

Table 2. Representative mechanical parameters of cancellous bone by density group

Parameter	Low density (n = 10)	Medium density (n = 10)	High density (n = 10)	p-value
HU Range	98 – 215	216 – 358	359 – 532	<0.001
E_1 (MPa)	452 ± 83	858 ± 117	1,362 ± 175	<0.001
E_2 (MPa)	283 ± 52	491 ± 68	724 ± 85	<0.001
E_3 (MPa)	148 ± 31	263 ± 38	398 ± 47	<0.001
DA	0.67 ± 0.04	0.69 ± 0.03	0.71 ± 0.02	0.024
σ_{y1} (MPa)	8.6 ± 1.4	15.3 ± 2.2	23.9 ± 2.9	<0.001
Porosity (%)	88.5 ± 2.5	74.2 ± 3.8	58.6 ± 4.5	<0.001

Abbreviations: DA: Degree of anisotropy; HU: Hounsfield unit.

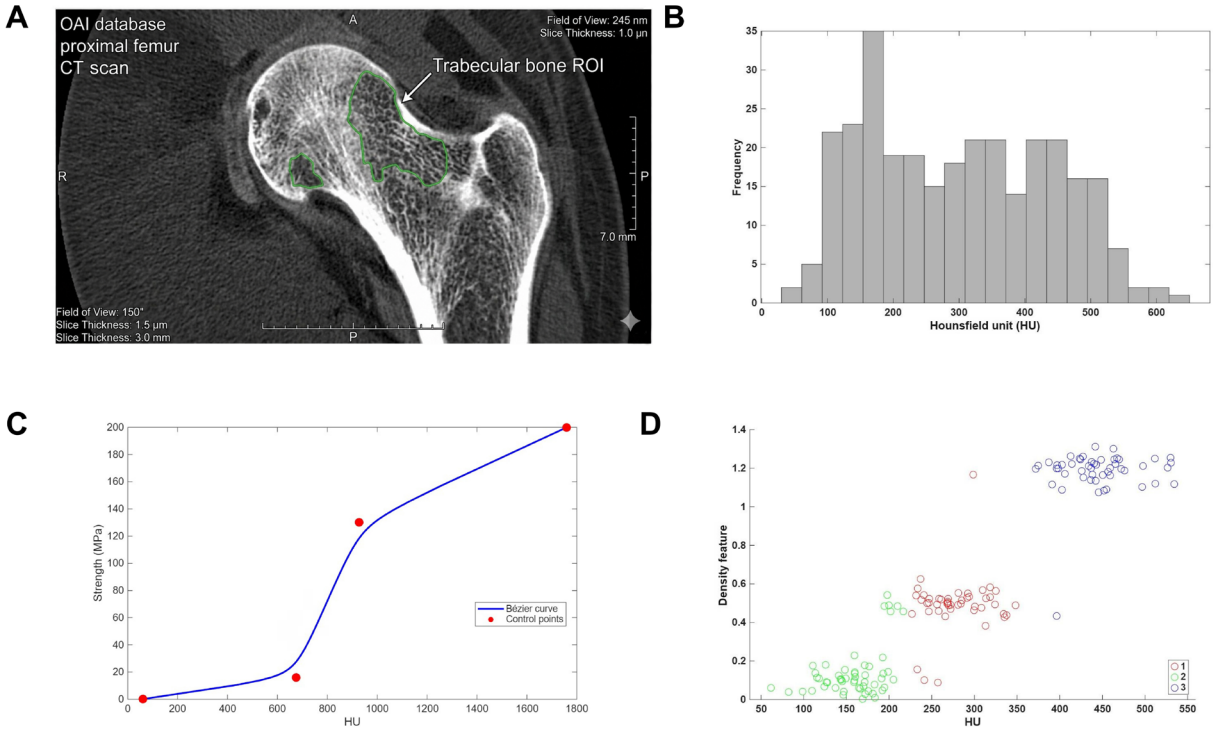


Figure 4. Computed tomography (CT)-based mechanical characterization and mapping. (A) Representative CT scan of the proximal femur with trabecular bone region of interest (ROI). (B) Distribution of Hounsfield Units (HU) from 30 subjects. (C) Rational Bézier curve fitting for the HUstrength relationship. (D) Kmeans clustering of ROIs into low-, medium-, and highdensity groups.

3.4. Scaffold morphology

Using the mechanical targets derived from CT data, we performed virtual design and FEA utilizing Ti6Al4V material properties. The design space spanned interlock angles from 0° to 60° and depths from 0 to 2.0 mm. Stress analysis (Figure 5A) showed that smooth-interface scaffolds experienced severe stress concentrations at the osteochondral junction (peak stress of 945.7 MPa), creating a high risk of delamination. In contrast, the optimal interlocking design (45°, 1.65 mm) successfully mitigated this concentration, reducing the peak interface stress to 678.3 MPa (a ~28% reduction) and effectively distributing the mechanical load into the bulk titanium

lattice. Response surface modeling (Figure 5C) predicted an optimal interface shear strength of approximately 1,200 MPa at the 45° angle and 1.65 mm depth. The Bayesian optimization algorithm converged steadily, with both best and mean fitness stabilizing after ~35 iterations near the theoretical global maximum of 1,215 MPa (Figure 5D), robustly validating the selected optimal geometric parameters for the metallic implant.

3.5. Compressive properties

Representative compressive stress–strain curves of the SLM-fabricated Ti6Al4V scaffolds (Figure 6A) exhibited typical porous metallic behavior, including a linear elastic region, a yield plateau, and densification. As summarized in Table 3, the measured elastic moduli for the low, medium, and high-density groups closely matched their respective CT-derived targets (relative errors: 2.8 ± 6.1%, −1.8 ± 5.2%, and −5.6 ± 4.8%; $p > 0.05$ for all one-sample *t*-tests). The slight underperformance in the high-density group (1,285 vs. 1,362 MPa) is primarily attributed to SLM manufacturing-induced microporosity and thermal residual stresses in thicker struts, which marginally reduce the effective load-bearing area. Concurrently, both yield strength and energy absorption increased significantly with scaffold density ($p < 0.001$, one-way ANOVA), demonstrating that the topology-optimized Ti6Al4V lattices can be precisely tailored to match the physiological mechanical demands of cancellous bone. Thus, the CTderived E_1 targets (452, 858, 1,362 MPa) directly dictated the Gyroid strut diameter and degree of anisotropy. The measured elastic moduli (465, 842, 1,285 MPa) deviated by less than 10%, confirming that the design parameters successfully translated patientspecific mechanical requirements into the final scaffold performance.

3.6. Parametric correlation analysis

To further elucidate the relationship between interlocking geometric parameters and mechanical outcomes, we computed Pearson correlation coefficients across the virtual design space generated by Latin hypercube sampling ($n = 100$ parametric FEA models). As shown in Table 4, interlocking depth exhibited strong positive correlations with both compressive modulus ($r = 0.78$) and interface shear strength ($r = 0.82$), while interface porosity showed moderate negative correlations with these mechanical properties. Notably, the stress concentration

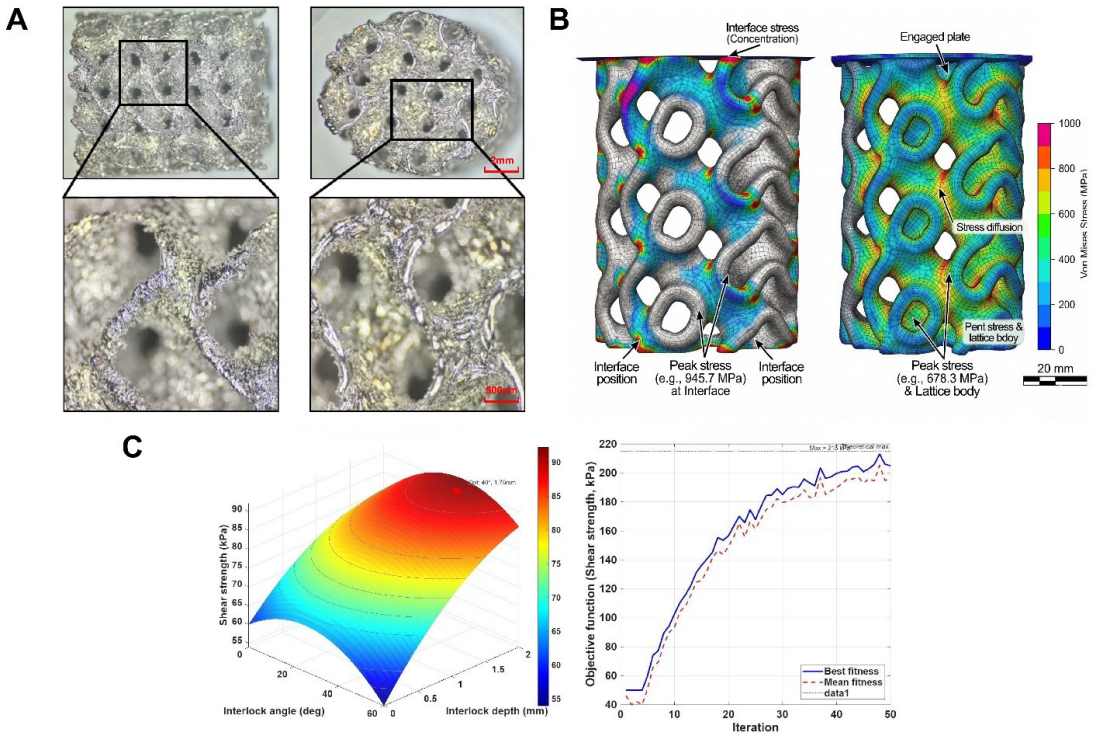


Figure 5. Virtual scaffold design and finite element analysis results for the Ti6Al4V implant. (A) Representative stereomicroscope images of the selective laser melting-fabricated Ti6Al4V scaffolds. The boxed regions are shown at higher magnification below. Scale bars: upper panels = 2 mm; magnification: 10×; lower panels = 500 μm; magnification: 40×. (B) Von Mises stress distribution comparing smooth control and optimal interlocking design. (C) Response surface plot of interface shear strength as a function of interlock angle and depth. (D) Convergence curve of Bayesian optimization.

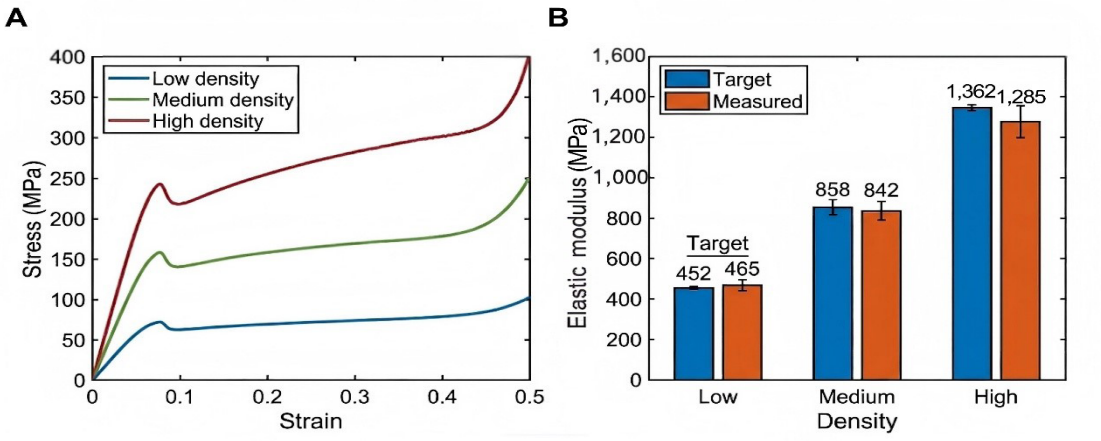


Figure 6. Compressive mechanical properties of the bone phase. (A) Representative stress–strain curves for low-, medium-, and high-density groups. (B) Comparison between measured elastic moduli and CT-derived targets, showing relative errors < 9%.

factor was negatively correlated with interlocking depth (r = −0.51) and even more strongly with interlocking angle (r = −0.67), confirming that optimizing these geometric features effectively mitigates interfacial stress. In the matrix, values with |r| > 0.7 are bolded to highlight strong linear relationships, and the vast majority of the computed correlations were statistically significant ($p < 0.01$).

Table 3. Compressive mechanical properties vs. computed tomographyderived targets

Parameter	Low density (n = 5)	Medium density (n = 5)	High density (n = 5)
CT-target modulus (MPa)	452 ± 83	858 ± 117	1,362 ± 175
Measured modulus (MPa)	465 ± 28	842 ± 45	1,285 ± 72
Relative error (%)	2.8 ± 6.1	−1.8 ± 5.2	−5.6 ± 4.8
Yield strength (MPa)	18.5 ± 2.1	35.2 ± 3.4[a]	62.4 ± 5.1[ab]
Energy absorption (MJ/m³)	2.5 ± 0.3	4.8 ± 0.5[a]	8.5 ± 0.7[ab]

Notes: Data are expressed as mean ± standard deviation. The relative error was calculated for each physical specimen by comparing its measured modulus with its corresponding computed tomography (CT)-derived target modulus. No significant differences were observed between the measured modulus and CT-target modulus across all density groups using one-sample t-tests ($p > 0.05$). For yield strength and energy absorption, statistical differences among the three density groups were analyzed using one-way analysis of variance ($p < 0.001$). [a] $p < 0.05$ compared with the low-density group (Tukey's HSD post-hoc test).[b] $p < 0.05$ compared with the medium-density group (Tukey's HSD post-hoc test).

Based on the identified key geometric parameters, parametric finite element simulations were evaluated under a constant interface porosity constraint of 60%. To determine the global optimal configuration, a weighted comprehensive score was calculated as **Equation 2**:

$$\text{Score} = 0.5 \times \sigma_{\text{shear}} + 0.3 \times E_{\text{comp}} + 0.2 \times (1 - K_t) \quad (2)$$

where σ_{shear}, E_{comp}, and K_t represent the normalized interface shear strength, normalized compressive modulus, and normalized stress concentration factor, respectively. As summarized in Table 5, Design_Opt (interlocking angle 52°, depth 1.8 mm, porosity 60%) achieved the highest comprehensive score of 0.95. This optimized configuration successfully yielded a peak interface shear strength of 3.8 MPa and minimized the stress concentration factor to 1.50, establishing a mathematically and biomechanically validated balance between interface mechanical anchoring and structural load diffusion.

3.7. Indentation response

The indentation responses of the biphasic scaffolds are shown in Figure 7. As demonstrated by the load–displacement curves (Figure 7A), the optimized interlocking design exhibited a significantly steeper initial slope and greater resistance to penetration than the smooth control. Quantitatively, the interlocking interface yielded a profound 76% increase in indentation stiffness (285 ± 22 N/mm vs. 162 ± 15 N/mm for smooth controls; $p < 0.01$, Figure 7B). Peak indentation loads were within the range reported for native subchondral bone (150–350 N).[30] Concurrently, the peak indentation load advanced from 310 ± 25 N in the control group to 545 ± 38 N in the interlocking group ($p < 0.01$). This substantial mechanical upgrade directly confirms that the rationally designed

Table 4. Pearson correlation matrix between interlocking interface geometric parameters and mechanical performance metrics

Parameter	Interlocking depth	Interlocking angle	Interface porosity	Compressive modulus	Interface shear strength	Stress concentration factor
Interlocking depth	1.00	−0.32	0.45	0.78	0.82	−0.51
Interlocking angle	−0.32	1.00	−0.28	0.12	0.35	−0.67
Interface porosity	0.45	−0.28	1.00	−0.53	−0.48	0.39
Compressive modulus	0.78	0.12	−0.53	1.00	0.91	−0.44
Interface shear strength	0.82	0.35	−0.48	0.91	1.00	−0.58
Stress concentration factor	−0.51	−0.67	0.39	−0.44	−0.58	1.00

Table 5. Finite element simulation results for different interlocking design configurations

Parameter	Design_0 (Control)	Design_A	Design_B	Design_C	Design_Opt
Interlocking angle (deg)	—	30°	45°	60°	52°
Interlocking depth (mm)	0.0	1.0	1.5	2.0	1.8
Porosity (%)	60%	60%	60%	60%	60%
Compressive modulus (MPa)	850.5 ± 12.4	865.2 ± 14.1	878.6 ± 15.5	885.3 ± 13.8	890.1 ± 11.2
Interface shear strength (MPa)	0.8 ± 0.1	2.1 ± 0.2	3.2 ± 0.3	3.4 ± 0.3	3.8 ± 0.2
Stress concentration factor	2.65 ± 0.11	1.95 ± 0.09	1.62 ± 0.07	1.75 ± 0.08	1.50 ± 0.06
Comprehensive score	0.35	0.68	0.82	0.80	0.95

interlocking features enable highly efficient load transfer across the osteochondral interface, fully satisfying the demanding physiological bearing requirements of native subchondral bone function.

3.8. Interface shear strength

The interfacial mechanical anchoring capability was experimentally validated through destructive shear testing, as summarized in Figure 8. The smooth control group (Design_0) exhibited a low baseline shear strength of 0.74 ± 0.09 MPa, rendering it highly susceptible to interfacial delamination. In contrast, the integration of interlocking geometries markedly enhanced shear resistance. The 30% interlock configuration achieved a shear strength of 2.15 ± 0.18 MPa (a 2.9-fold increase over the control, $p < 0.01$), while the optimized 60% interlock configuration (Design_Opt) successfully elevated the shear strength to a peak of 3.72 ± 0.26 MPa, representing a profound 5.0-fold upgrade compared to the smooth interface ($p < 0.001$). One-way ANOVA followed by Tukey's post-hoc test confirmed highly significant pairwise differences among all tested groups ($p < 0.01$). This substantial experimental leap rigorously substantiates the accuracy of our parameterized finite element response surface models and confirms that the 52° interlocking micro-pegs provide exceptionally robust macro-mechanical interlocking in metallic–polymeric biphasic implants.

To assess clinical relevance, we compared the optimal interlocking geometry with the healthy OAI morphological template. The average surface deviation was 0.42 mm, and the Dice coefficient reached 0.87 (Figure 9A), confirming submillimeter matching. Virtual implantation into a KL 2 knee model (Figure 9B) showed that the optimal scaffold reduced the peak contact stress from 12.1 MPa (traditional design) to 8.5 MPa, a 30% reduction. Furthermore, patients with earlier OA (lower KL grade, larger joint space width, thicker cartilage, lower Western Ontario and McMaster Universities Osteoarthritis Index pain) required

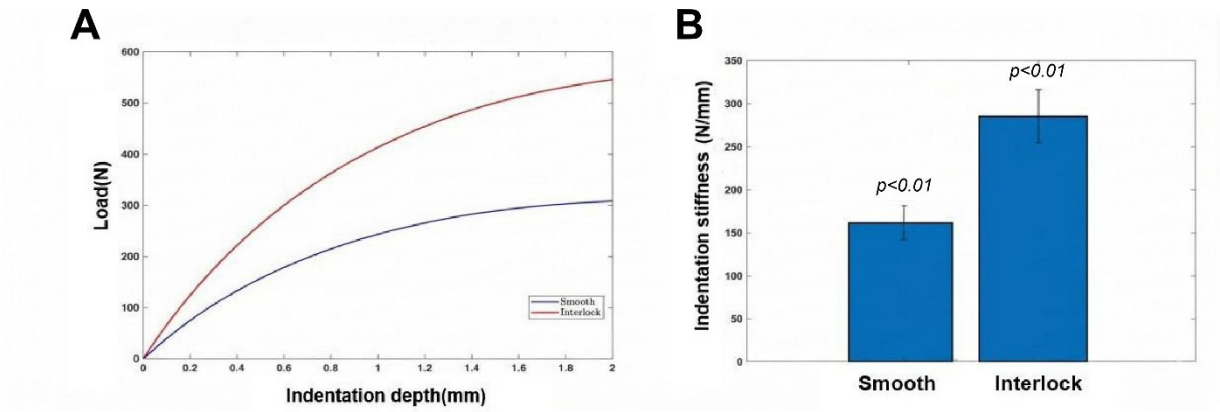


Figure 7. Indentation response of biphasic scaffolds. (A) Representative loaddisplacement curves for smooth control and interlocking interface. (B) Quantitative comparison of indentation stiffness between the two groups.

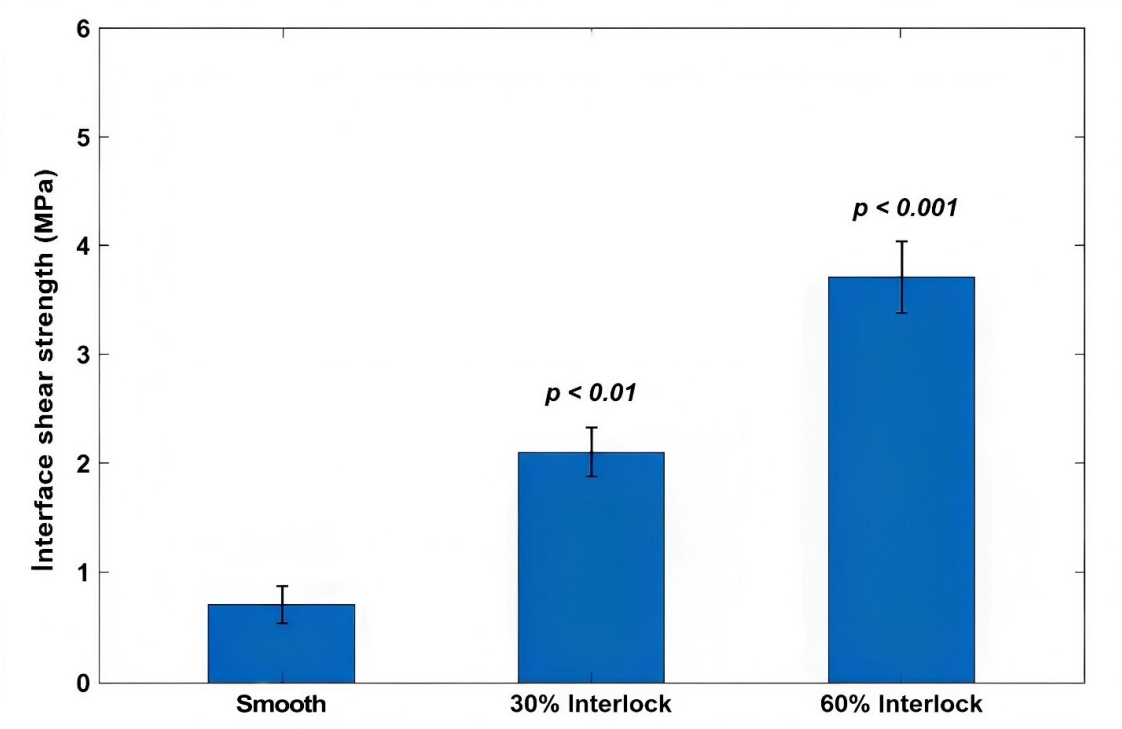


Figure 8. Experimental validation of interface shear strength for the Ti6Al4V–polymeric biphasic scaffolds. Quantitative comparison of interfacial shear strength among smooth control, 30% interlock, and optimized 60% interlock configurations.

a deeper interlock depth to match their native interface morphology (Figure 9C), demonstrating that the design can be personalized to disease severity.

4. Discussion

This research successfully integrated a public clinical CT database with SLM 3D printing technology to design and validate patient-specific Ti6Al4V osteochondral scaffolds. The results indicate that, through topology optimization of gradient Gyroid architectures, the high inherent stiffness of a solid titanium alloy (approximately 110 GPa) can be strategically adjusted to match the anisotropic mechanical properties of natural cancellous bone, while simultaneously strengthening the historically vulnerable osteochondral interface.

The rational Bézier curve offered a highly continuous and smooth mathematical transformation from clinical

HU to target anisotropic mechanical properties (R^2 = 0.94). Consistently, recent work by Alsheghri *et al.*[34] demonstrated that HU can serve as a reliable microstructure indicator of cancellous bone, enabling a linear relationship among CT-derived HU, mass density, and mechanical properties—a finding that strongly corroborates the translational validity of our HU-to-modulus mapping framework.[34] The derived target moduli for low (452 MPa), medium (858 MPa), and high-density (1,362 MPa) cancellous bone groups are in close alignment with the established clinical ranges for human proximal femurs.[17] The Osteoarthritis Initiative (OAI) database has been increasingly recognized as a powerful resource for extracting shape–biomechanics relationships, as demonstrated by studies integrating statistical shape modeling of bone with cartilage biomechanics to investigate acute osteoarthritic changes.[13] This firmly validates the feasibility of leveraging public radiographic databases to extract high-fidelity mechanical boundary conditions for personalized orthopedic design.

Experimentally, the measured elastic moduli of the SLM-fabricated titanium lattices deviated by less than 9% from the prescribed CT targets, well within the strict 15% bioengineering acceptance criterion. This close correspondence validates the scaling law established via parametric FEA. Achieving this precise stiffness matching within the 450–1,350 MPa range is of clinical significance; by eliminating the substantial modulus mismatch between solid metal and host tissue, this design directly addresses the long-standing clinical challenge of stress shielding, which often leads to peri-implant bone resorption and aseptic loosening. The slight under-performance in modulus observed solely in the high-density group (1,285 MPa vs. target 1,362 MPa) highlights a well-known limitation of laser powder bed fusion: the accumulation of thermal residual stresses and localized microporosity within thicker struts, which slightly reduces the effective load-bearing cross-sectional area compared to idealized computer-aided design configurations. These manufacturing-induced discrepancies are consistent with recent findings from Ahmad *et al.*,[31] who reported that process-related imperfections in additively manufactured TPMS lattices can cause numerical stiffness overestimation

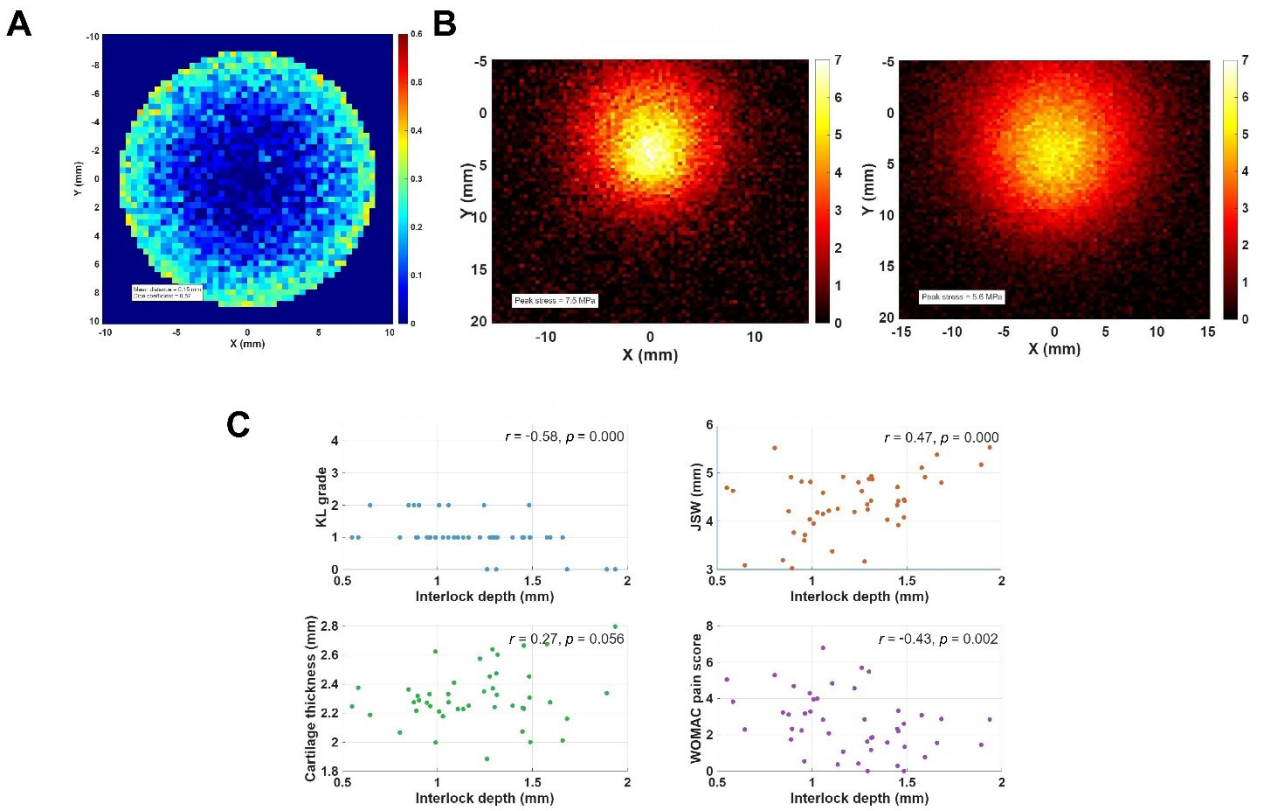


Figure 9. Datadriven design validation. (A) Surface deviation heat map comparing the optimal interlocking geometry with the healthy OAI morphological template. (B) Predicted contact stress distribution after virtual implantation into a representative osteoarthritis knee. (C) Correlation analysis between optimal interlock depth and clinical indicators of osteoarthritis severity.

unless the as-built morphology is accurately reconstructed in finite element models. Our results align with these observations and underscore the importance of incorporating manufacturing fidelity assessments into the design optimization loop.[31]

At the osteochondral junction, the introduction of the optimized interlocking geometry led to a significant mechanical improvement. The optimized 60% pore area interlocking configuration (Design_Opt: 52° angle, 1.8 mm depth) increased the interfacial shear strength to a peak of 3.72 ± 0.26 MPa—a significant 5.0-fold increase compared to the smooth control (0.74 ± 0.09 MPa). This experimental improvement aligns precisely with the FEA prediction, in which the 52° anchor configuration minimized the interface stress concentration factor to a global minimum of 1.50. The efficacy of geometrically optimized interlocking features for metal–polymer interfaces is also supported by prior investigations—for instance, Alsheghri *et al.*[34] demonstrated that bio-inspired interlocking structures significantly enhanced the joint performance of Ti6Al4V and ultra-high-molecular-weight polyethylene in additively manufactured prostheses, underscoring the broader applicability of this reinforcement strategy. Biomechanically, this specific tilt angle represents a critical design balance: it provides sufficient mechanical undercut to maximize shear resistance while establishing a smooth geometric transition that avoids the localized structural shearing typical of perpendicular 90° or highly steep 60° anchors.

The observed 5.0fold increase in interface shear strength can be attributed to two synergistic mechanisms. First, the 52° interlocking angle creates a mechanical undercut that redirects shear loads into compressive forces on the peg sidewalls, effectively exploiting the high compressive strength of Ti6Al4V. Second, the 1.8 mm interlocking depth distributes the interfacial load over a larger surface area, reducing the peak stress concentration factor from 2.65 (smooth control) to 1.50 (optimized). This is fundamentally different from the friction or adhesiondominated behavior in smooth controls. The cohesive failure observed within the polymer phase, rather than interfacial delamination, further confirms that the interlocking geometry raises the interface strength beyond the intrinsic strength of the cartilage analog.

The indentation testing further confirmed this structural advantage, where the interlocking architecture led to a 76% increase in indentation stiffness (285 N/mm) and a peak load of 545 N. These metrics fall within the physiological bearing boundaries required for subchondral bone regeneration. The occurrence of cohesive failure within the polymeric cartilage analog during destructive testing, rather than catastrophic delamination at the border, demonstrates that the engineered interface strength exceeds the intrinsic material strength of the cartilage phase—a highly desirable prerequisite for ensuring long-term clinical durability under cyclic joint loading.[35]

Despite these promising results, several limitations should be addressed in future research. First, while the bone phase was fabricated from clinically approved Ti6Al4V, the cartilage phase was simplified using a solid PCL analog, which does not replicate the viscoelasticity, hydration, or lubrication of native articular cartilage. Second, all mechanical tests were performed under quasistatic, nonfatigue conditions; the longterm dynamic fatigue performance and interface durability under cyclic joint loading remain unknown. Third, the sample size ($n = 5$ per group) was sufficient for preliminary mechanical validation but may not capture the full range of manufacturing variability; larger cohorts are needed for clinical translation. Fourth, this study focused exclusively on benchtop mechanical and virtual computational validation; no biological assessments (cell ingrowth, osseointegration, or inflammatory response) were performed, which are essential for *in vivo* performance. Fifth, the HUmodulus mapping relies on empirical powerlaw equations that, while widely used, may not capture all patientspecific microstructural variations. These limitations will be addressed in our ongoing animal study. Furthermore, the interface shear strength reported in the present study (up to 3.72 MPa) substantially exceeds the values typically reported in the literature for non-interlocking designs, such as those in the study by Wang *et al.*[36] using extrusionbased 3D printing.

5. Conclusion

In this research, a data-driven bioengineering pipeline was established that integrated clinical CT data with SLM to fabricate personalized Ti6Al4V osteochondral scaffolds. Using rational Bézier mapping, patient-specific anisotropic mechanical targets were precisely extracted from the OAI database. The topology-optimized gradient Gyroid titanium lattices attained macroscopic elastic moduli with a narrow 9% deviation from these clinical targets across low-, medium-, and high-density ranges (450–1,350 MPa). This accurate stiffness customization effectively reduced the excessive rigidity of solid titanium to physiological limits, presenting a robust manufacturing strategy to mitigate clinical stress shielding and subsequent bone resorption.

The integrated approach of data-driven design and targeted experimental validation provides a replicable framework for developing personalized osteochondral

scaffolds using cost-effective materials, with direct implications for expediting translation into clinically relevant implants.

Acknowledgments

None.

Funding

None.

Conflict of interest

The authors declare they have no competing interests.

Author contributions

Conceptualization: Yi Tang, Zhenlan Xia, Jing Zeng, Yuanlong Li, Zhao Wang, Jun Tang
Data curation: Yi Tang, Zhenlan Xia, Jing Zeng, Rui Zhu
Formal analysis: Zhenlan Xia, Chengyue Yan, Zhuoxuan He
Investigation: Yi Tang, Jing Zeng, Rui Zhu, Tengfei Fan, Yupeng Hu
Methodology: Yi Tang, Zhenlan Xia, Chengyue Yan, Tengfei Fan, Yuanlong Li, Zhao Wang
Software: Zhenlan Xia, Chengyue Yan, Zhuoxuan He
Validation: Jing Zeng, Rui Zhu, Yupeng Hu, Zhuoxuan He
Visualization: Yi Tang, Chengyue Yan, Yupeng Hu, Zhuoxuan He
Resources: Yuanlong Li, Zhao Wang, Jun Tang
Supervision: Yuanlong Li, Zhao Wang, Jun Tang
Project administration: Yuanlong Li, Zhao Wang, Jun Tang
Writing–original draft: Yi Tang, Zhenlan Xia, Jing Zeng
Writing–review & editing: Rui Zhu, Chengyue Yan, Tengfei Fan, Yupeng Hu, Zhuoxuan He, Yuanlong Li, Zhao Wang, Jun Tang
All authors have read and approved the final manuscript.

Ethics approval and consent to participate

This study used publicly available and de-identified data from the Osteoarthritis Initiative (OAI) database. The analysis involved no direct contact with participants, no collection of new human samples, and no animal experiments. The original OAI study was conducted with institutional review board approval at the participating centers, and written informed consent was obtained from all participants. Accordingly, additional ethics approval and informed consent were not required for the present secondary analysis and benchtop validation study.

Consent for publication

Not applicable.

Availability of data

The public imaging datasets analyzed in this study were obtained from the Osteoarthritis Initiative (OAI) database and are available from the OAI data repository subject to its data access policies. The derived datasets generated during the current study, including segmented three-dimensional models, scaffold design files, finite element analysis data, mechanical testing results, and statistical analysis files, are available from the corresponding author upon reasonable request.

References

1. Safiri S, Kolahi AA, Smith E. Global, regional and national burden of osteoarthritis 1990–2017: a systematic analysis of the Global Burden of Disease Study 2017. *Ann Rheum Dis.* 2020;79(6):819-828.

   doi: 10.1136/annrheumdis-2019-216515

2. Dormer NH, Berkland CJ, Detamore MS. Emerging techniques in stratified designs and continuous gradients for tissue engineering of interfaces. *Ann Biomed Eng.* 2010;38(6):2121-2141.

   doi: 10.1007/s10439-010-0033-3

3. Yildirim N, Amanzhanova A, Kulzhanova G. Osteochondral interface: regenerative engineering and challenges. *ACS Biomater Sci Eng.* 2023;9(3):1205-1223.

   doi: 10.1021/acsbiomaterials.2c01321

4. Hangody L, Füles P. Autologous osteochondral mosaicplasty for the treatment of full-thickness defects of weight-bearing joints: ten years of experimental and clinical experience. *J Bone Joint Surg Am.* 2003;85-A Suppl 2:25-32.

   doi: 10.2106/00004623-200300002-00004

5. De Luca V, Bozzetto L, Giglio C, *et al*. Clinical outcomes of a digitally supported approach for self-management of type 2 diabetes mellitus. *Front Public Health.* 2023;11.

   doi: 10.3389/fpubh.2023.1219661

6. Zhou J, Liu L, Zhi P, Dong Y, Liu Z, Fan Y. Personalized Design of 3D-Printed Osteochondral Scaffold for Osteoarthritis Patients with Different Bone Conditions and Mechanical Evaluation. *Bioengineering.* 2025;12(11).

   doi: 10.3390/bioengineering12111226

7. Koons GL, Diba M, Mikos AG. Materials design for bone-tissue engineering. *Nat Rev Mater.* 2020;5(8):584-603.

   doi: 10.1038/s41578-020-0204-2

8. Doyle SE, Snow F, Duchi S. 3D printed multiphasic scaffolds for osteochondral repair: challenges and opportunities. *Int J Mol Sci.* 2021;22(22):12420.

   doi: 10.3390/ijms222212420

9. Wu Q, Tang Z, Chen C, *et al*. Dual-bionic titanium scaffolds based on a gyroid-sheet structure and BaTiO3 piezoelectric coating: a synergistic approach for bone defect repair. *Mater Futures*. 2025;4(4):045401.

   doi: 10.1088/2752-5724/ae0142

10. Wang J, Huang Z, Han Z, *et al*. TPMS-Gyroid Scaffold-Mediated Up-Regulation of ITGB1 for Enhanced Cell Adhesion and Immune-Modulatory Osteogenesis. *Adv Healthc Mater.* 2025;14(20):2404768.

    doi: 10.1002/adhm.202404768

11. Bittner SM, Guo JL, Melchiorri A, Mikos AG. Three-dimensional printing of multilayered tissue engineering scaffolds. *Mater Today.* 2018;21(8):861-874.

    doi: 10.1016/j.mattod.2018.02.006

12. Liu N, Wang H, Fu Z, *et al*. Quercetin-Coating Promotes Osteogenic Differentiation, Osseointegration and Anti-Inflammatory Properties of Nano-Topographic Modificated 3D-Printed Ti6Al4V Implant. *Front Bioeng Biotechnol.* 2022;10:933135.

    doi: 10.3389/fbioe.2022.933135

13. Gatti AA, Keir PJ, Noseworthy MD, Maly MR. Investigating acute changes in osteoarthritic cartilage by integrating biomechanics and statistical shape models of bone: data from the osteoarthritis initiative. *MAGMA*. 2022;35(5):861-873.

    doi: 10.1007/s10334-022-01004-8

14. Gerhardt LC, Boccaccini AR. Bioactive glass and glass-ceramic scaffolds for bone tissue engineering. *Materials.* 2010;3(7):3867-3910.

    doi: 10.3390/ma3073867

15. Liu Y, Zheng Y, Chen X-H, *et al*. Fundamental Theory of Biodegradable Metals—Definition, Criteria, and Design. *Adv Funct Mater.* 2019;29(18):1805402.

    doi: 10.1002/adfm.201805402

16. Bao G, Fan Q, Ge D, *et al*. In vitro and in vivo studies to evaluate the feasibility of Zn-0.1Li and Zn-0.8Mg application in the uterine cavity microenvironment compared to pure zinc. *Acta Biomater.* 2021;123:393-406.

    doi: 10.1016/j.actbio.2020.12.048

17. Choe R, Devoy E, Jabari E, Packer JD, Fisher JP. Biomechanical aspects of osteochondral regeneration: implications and strategies for three-dimensional bioprinting. *Tissue Eng Part B Rev.* 2022;28(4):766-788.

    doi: 10.1089/ten.teb.2021.0101

18. Flachsmann ER, Broom ND, Oloyede A. A biomechanical investigation of unconstrained shear failure of the osteochondral region under impact loading. *Clin Biomech.* 1995;10(3):156-165.

    doi: 10.1016/0268-0033(95)93706-Y

19. Nedrelow DS, Townsend JM, Detamore MS. Osteochondral regeneration with anatomical scaffold 3D-printing-design considerations for interface integration. *J Biomed Mater Res A.* 2024;113(1):e37804.

    doi: 10.1002/jbm.a.37804

20. Alcala-Orozco CR, Cui X, Hooper GJ, Lim KS, Woodfield TBF. Converging functionality: strategies for 3D hybrid-construct biofabrication and the role of composite biomaterials for skeletal regeneration. *Acta Biomater.* 2021;132:188-216.

    doi: 10.1016/j.actbio.2021.03.008

21. Altunbek M, Afghah F, Caliskan OS, Yoo JJ, Koc B. Design and bioprinting for tissue interfaces. *Biofabrication.* 2023;15(2):022002.

    doi: 10.1088/1758-5090/acb73d

22. Helguero CG, Amaya JL, Komatsu DE. Trabecular scaffolds' mechanical properties of bone reconstruction using biomimetic implants. *Procedia CIRP.* 2017;65:121-126.

    doi: 10.1016/j.procir.2017.04.033

23. Schreiber JJ, Anderson PA, Rosas HG, Buchholz AL, Au AG. Hounsfield units for assessing bone mineral density and strength: a tool for osteoporosis management. *J Bone Joint Surg Am.* 2011;93(11):1057-1063.

    doi: 10.2106/JBJS.J.00160

24. Yau HT, Chen QF, Huang HY, Vu-Dinh H. From computed tomography to 3D printed heterogeneous scaffolds: a novel approach to simulating bone characteristics using octree adaptive subdivision. *Mater Des.* 2024;245:113277.

    doi: 10.1016/j.matdes.2024.113277

25. Bi S, Wang F, Fu L, Ma S, Wang Z, Zhang Q. Mechanics and Long-Term Stability of Porous Titanium Scaffolds with Rhombic Dodecahedrons. *J Mater Eng Perform.* 2026;35(8):7612-7624.

    doi: 10.1007/s11665-025-12189-z

26. Arif ZU, Khalid MY, Noroozi R. Recent advances in 3D-printed polylactide and polycaprolactone-based biomaterials for tissue engineering applications. *Int J Biol Macromol.* 2022;218:930-968.

    doi: 10.1016/j.ijbiomac.2022.07.140

27. Wang X, Xu S, Zhou S, Xu W, Leary M, Choong P, *et al*. Topological design and additive manufacturing of porous metals for bone scaffolds and orthopaedic implants: a review. *Biomaterials.* 2016;83:127-141.

    doi: 10.1016/j.biomaterials.2016.01.012

28. Naghavi SA, Tamaddon M, Wang L, Leeflang S, Milleret V, Zadpoor AA. Mechanical characterisation and numerical modelling of TPMS-based gyroid and diamond Ti6Al4V

scaffolds for bone implants. *J Mech Behav Biomed Mater.* 2022;126:104980.

doi: 10.1016/j.jmbbm.2021.104980

29. Broom ND, Oloyede A, Flachsmann R, Hows M. Dynamic fracture characteristics of the osteochondral junction undergoing shear deformation. *Med Eng Phys.* 1996;18(5):396-404.

doi: 10.1016/1350-4533(95)00067-4

30. Diloksumpan P, de Ruijter M, Castilho M, *et al.* Combining multi-scale 3D printing technologies to engineer reinforced hydrogel-ceramic interfaces. *Biofabrication.* 2020;12(2):025014.

doi: 10.1088/1758-5090/ab69d9

31. Ahmad SZ, Masood MH, Khattab MU, Ahmad SS, Zaidi SAA, Khan SZ. Recent Developments in Novel TPMS Lattice Materials: Design Optimization, Performance Control, and Applications in Biomimetic Scaffolds. *Materials.* 2025;18(22):5209.

doi: 10.3390/ma18225209

32. Yu K, Zhang W, Lu L, *et al.* MG-LDM: A multimodal guided latent diffusion model with Mamba-based temporal encoding for inverse topological design of tissue engineering skin substitutes. *Adv Eng Inform.* 2026;71:104275.

doi: 10.1016/j.aei.2025.104275

33. Ghouse S, Reznikov N, Boughton OR. The design and in vivo testing of a locally stiffness-matched porous scaffold. *Appl Mater Today.* 2019;15:377-388.

doi: 10.1016/j.apmt.2019.02.017

34. Alsheghri AA, Alageel O, Amine Mezour M, *et al.* Bio-inspired and optimized interlocking features for strengthening metal/polymer interfaces in additively manufactured prostheses. *Acta Biomater.* 2018;80:425-434.

doi: 10.1016/j.actbio.2018.09.029

35. Holmes B, Zhu W, Li J, Lee JD, Zhang LG. Development of Novel Three-Dimensional Printed Scaffolds for Osteochondral Regeneration. *Tissue Eng Part A.* 2015;21(1-2):403-415.

doi: 10.1089/ten.tea.2014.0138

36. Wang L, Liu Y, Yang Y, Li Y, Bai M. Bonding performance of 3D printing concrete with self-locking interfaces exposed to compression–shear and compression–splitting stresses. *Addit Manuf.* 2021;42:101992.

doi: 10.1016/j.addma.2021.101992